https://doi.org/10.5194/egusphere-2026-2230
Preprint. Discussion started: 27 July 2026

Development of a dual-polarization Zdr radar operator with ice-phase hydrometeor classification for variational assimilation systems (RadDualIceVar v1.0)

Liu Yi[1,2], Feifei Shen[1,2,3,5*] Zhixin He[4], and Dongmei Xu[1,2]

[1]Key Laboratory of Meteorological Disaster, Ministry of Education (KLME) /Joint International Research Laboratory of Climate and Environment Change (ILCEC) /Collaborative Innovation Center on Forecast and Evaluation of Meteorological Disasters (CIC-FEMD), Nanjing University of Information Science & Technology, Nanjing 210044, China

[2] Key Laboratory of Liuzhou Yuanbaoshan Topography Heavy Rain, Zhou Liu, 545000, China

[3]Chongqing Key Laboratory of Numerical Model-AI Integrated Forecast and Warning for Severe Weather, 40000, China

[4]Anhui Meteorological Observatory, Hefei 230000, China

[5]Key Laboratory of Transportation Meteorology of China Meteorological Administration, Nanjing Joint Institute for Atmospheric Sciences, Nanjing 210041, China

Correspondence to: Feifei Shen(ffshen@nuist.edu.cn)

Abstract. A differential reflectivity (Zdr) observation operator incorporating ice-phase hydrometeor classification was developed to explicitly account for ice-phase hydrometeor contributions in the data assimilation. This proposed observation operator is then implemented within a three-dimensional variational (3DVAR) data assimilation framework for direct assimilating radar Zdr observations. Its performance was evaluated using both single-observation and cycling assimilation experiments for a typhoon case. Results from the single-observation test indicate that assimilating Zdr introduces additional microphysical constraints, leading to more effective adjustments of hydrometeor compared with reflectivity-only assimilation. In the cycling assimilation experiments, the combined reflectivity and Zdr (RFZDR) configuration produces a more physically consistent representation of reflectivity and Zdr, along with a more realistic vertical and horizontal distribution of hydrometeors. These improvements propagate into short-term precipitation forecasts, with RFZDR exhibiting lower root-mean-square errors, enhanced spatial consistency, and gains in heavy precipitation metrics.

1 Introduction

In modern Numerical Weather Prediction (NWP) systems, an accurate representation of initial conditions is essential for improving mesoscale and convective-scale forecasts, particularly in high-resolution modeling frameworks (Bauer et al., 2015). The Weather Research and Forecasting (WRF) model is one of the most widely used mesoscale numerical modeling systems. It has been extensively applied in both research and operational forecasting of severe convection, precipitation, and hazardous weather, owing to its flexible dynamical framework and comprehensive suite of physical parameterization schemes (Wang et al., 2013; Shen et al., 2021). Despite these advances, the effective assimilation of high-temporal- and high-spatial-resolution

https://doi.org/10.5194/egusphere-2026-2230
Preprint. Discussion started: 27 July 2026

observations to improve convective-scale initial condition analyses remains a major challenge. Among available observing systems, weather radar observations are particularly critical because they directly sample storm-scale dynamical and microphysical structures (Xiao and Sun, 2007; Hou et al., 2015).

Compared with conventional single-polarization Doppler radar, dual-polarization radar has substantially enhanced the capability of weather radar to probe cloud and precipitation microphysical processes (Carlin et al., 2017). Traditional Doppler radar transmits and receives signals only at horizontal polarization, whereas dual-polarization radar employs both horizontally and vertically polarized pulses. This configuration provides additional information on hydrometeor shape, orientation, and phase (Zhang et al., 2019). These polarimetric variables provide stronger physical constraints on hydrometeor identification and precipitation structure analysis, and they also introduce more informative and dynamically consistent observations into numerical data assimilation systems (Zhang et al., 2001; Jung et al., 2008).

Dual-polarization radar observations have been extensively applied in convective-scale research due to their advantages. These applications include hydrometeor classification (Dolan et al., 2013; Snyder et al., 2015), attenuation correction (Snyder et al., 2010), and quantitative precipitation estimation (Tabary et al., 2011). Distinct polarimetric signatures, including Zdr arcs, ρhv rings, and Kdp feet, have been identified and are associated with specific microphysical processes in convective storms (Zhang et al., 2019). Collectively, these efforts have advanced the understanding of precipitation structure and the microphysical evolution of convective systems.

In earlier studies, most dual-polarization radar assimilation efforts relied on indirect assimilation strategies, in which polarimetric information was incorporated through proxy variables rather than being assimilated explicitly (Chen et al., 2021). Because cross-covariances between the observed polarimetric quantities and all relevant model state variables are often weak or insufficiently represented, only a subset of the state variables can be effectively updated. Consequently, the resulting analyses may suffer from dynamical and thermodynamical imbalances (Putnam et al., 2021).

In recent years, the direct assimilation of dual-polarization radar observations has become an active area of research in convective-scale numerical prediction. Within the Ensemble Kalman Filter (EnKF) framework, Jung et al. (2008, 2010; hereafter J08) systematically developed observation operators for polarimetric radar variables, enabling the direct assimilation of Zdr and other dual-polarization variables. Their methodology was successfully demonstrated in idealized simulations of severe convective storms and laid an important foundation for incorporating polarimetric radar observations into numerical models. Nevertheless, EnKF generally requires relatively large ensemble sizes to maintain statistical robustness, leading to substantial computational costs in high-resolution, convective scale applications and posing challenges for operational implementation.

In contrast, variational data assimilation methods offer greater computational efficiency while maintaining physical consistency, and they have therefore attracted increasing attention in radar data assimilation. However, their application

https://doi.org/10.5194/egusphere-2026-2230
Preprint. Discussion started: 27 July 2026

critically depends on the development of tangent-linear (TL) and adjoint (AD) models for the corresponding observation operators, making the assimilation of dual-polarization radar observations particularly challenging. Kawabata et al. (2018) addressed this issue by implementing dual-polarization radar data assimilation within a variational framework through the development of consistent TL and AD operators. This work represents an important extension of polarimetric radar assimilation from EnKF-based to variational approaches.

From the perspective of cloud microphysical processes, most existing studies on dual-polarization radar data assimilation have primarily focused on warm-rain processes. Despite this importance, many existing observation operators provide only limited representation of ice-phase contributions. For example, the observation operator developed by Kawabata et al. (2018) considers only rain-phase hydrometeors and does not explicitly account for ice-phase effects. Although Chen et al. (2025) recently enhanced the analysis framework by incorporating hydrometeor variables into the background state, their observation operators are still tailored for warm-rain processes and lack explicit ice-phase treatments.

Prior research has established that ice-phase hydrometeors significantly modulate radar reflectivity structures in convective systems, particularly within the vertical dimension. Gao and Stensrud (2012) demonstrated that the explicit inclusion of ice-phase hydrometeors in reflectivity observation operators enhances the analysis of vertical structures. In convective systems such as typhoons, these ice-phase microphysical processes are indispensable for hydrometeor growth within outer rainbands (Wang et al., 2016; Wu et al., 2018). Within the EnKF framework, J08, building on the work of Zhang et al. (2001), developed a dual-polarization radar observation operator that accounts for both rain- and ice-phase hydrometeor contributions using a combination of the T-matrix method and the Rayleigh scattering approximation. However, such an approach has not yet been extended to variational data assimilation systems. Wang and Liu (2018), following the formulation of J08, investigated the impact of ice-phase hydrometeors within a three-dimensional variational (3DVAR) reflectivity assimilation framework, but dual-polarization radar variables were not considered.

In summary, within variational data assimilation frameworks, the direct assimilation of dual-polarization radar variables that explicitly account for ice-phase hydrometeor scattering remains an open research problem. Previous studies have primarily focused on warm-rain processes, with limited consideration of ice-phase and melting-layer contributions in the observation operators. To address this gap, the present study systematically incorporates ice-phase hydrometeor and melting-layer effects into the Zdr observation operator. Beyond a forward-model extension, a consistent TL and AD framework is developed, enabling its application within the iterative optimization of a 3DVAR system. The aim is to improve the analysis of convective-scale hydrometeor structures and to enhance numerical forecasts of precipitation and severe convective weather.

The remainder of this study is structured as follows. Section 2 details the development of radar reflectivity and Zdr operators, with an explicit emphasis on ice-phase hydrometeor treatments. The experimental design and datasets are described in Sect. 3. In Sect. 4, the performance of the proposed method is evaluated through a representative typhoon case. Finally, Sect.

https://doi.org/10.5194/egusphere-2026-2230
Preprint. Discussion started: 27 July 2026

5 summarizes the main findings and conclusions.

2 Polarimetric radar operators

2.1 J08 operator with ice-phase

2.1.1 The melting model and variables to polarimetric parameters

Following the J08 operator, the melting layer model simulates mixed-phase hydrometeors within the melting layer, such as melting snow. These mixed-phase particles are represented by a prescribed fraction (F) describing rain–snow and rain–graupel mixtures.

$$F = F_{\max}\left[\min(q_x / q_r, q_r / q_x)\right]^{0.3}, \tag{1}$$

where, F_{max} denotes the maximum fraction, which is prescribed as 0.5 for rain–snow mixtures and 0.3 for rain–graupel. The variables q_r and q_x represent the mixing ratios of rainwater and a generic ice-phase species, respectively, where the subscript x refers to either snow (s) or graupel (g). Based on these definitions, the mixing ratios for pure rainwater (q_{pr}), the dry ice-phase (q_{dx}), and the mixed-phase species (q_{wx}) are defined as follows:

$$\begin{aligned} q_{pr} &= (1 - F_{ws} - F_{wg})q_r, \\ q_{dx} &= (1 - F_{wx})q_x, \\ q_{wx} &= F_{wx}(q_x + q_r), \end{aligned} \tag{2}$$

where, F_{wx} denotes the fraction of mixed-phase hydrometeors. The density of the mixed-phase hydrometeors is expressed in terms of the densities of the ice-phase species and rainwater,

$$\rho_{wx} = (1 - f_{wx}^2)\rho_x + f_{wx}^2 \rho_r, \tag{3}$$

where f_{wx} representing the fraction of melting, is defined as:

$$f_{wx} = \frac{q_r}{q_r + q_x}. \tag{4}$$

The horizontally and vertically reflectivities ($Z_{H/V}$) are expressed as:

$$Z_{H/V} = 10\log_{10}(Z_{h/v}), \tag{5}$$

where $Z_{h/v}$ is the equivalent reflectivity factor. Therefore, following Gao and Stensrud (2012), the reflectivity observation operator is partitioned here based on the model temperature (T_b).

$$Z_{h/v} = \begin{cases} Z_{h/v}(q_{pr}), & T_b > 5^\circ C, \\ Z_{h/v}(q_{ds}) + Z_{h/v}(q_{dg}) + Z_{h/v}(q_{ws}) + Z_{h/v}(q_{wg}), & T_b < -5^\circ C, \\ \alpha Z_{h/v}(q_{pr}) + (1-\alpha)[Z_{h/v}(q_{ds}) + Z_{h/v}(q_{dg}) + Z_{h/v}(q_{ws}) + Z_{h/v}(q_{wg})], & -5^\circ C < T_b < 5^\circ C. \end{cases} \tag{6}$$

ZDR is defined as the logarithmic ratio of radar reflectivity measured at horizontal and vertical polarizations:

https://doi.org/10.5194/egusphere-2026-2230
Preprint. Discussion started: 27 July 2026

$$Z_{dr}=10\log_{10}\frac{Z_h}{Z_v}=Z_H-Z_V. \tag{7}$$

Jung et al. (2008) provided a detailed description of the formulas and parameters for reflectivity at horizontal ($Z_{h,x}$) and vertical ($Z_{v,x}$) polarizations, while Wang and Liu (2019) supplemented the parameters for graupel. The reflectivity at horizontal and vertical polarizations is obtained by integrating the drop size distribution (DSD) weighted by the scattering cross section, which depends on particle density, shape, and the DSD.

$$Z_{h,x}=\frac{4\lambda^4}{\pi^4|K_w|^2}\int n(D)(A|f_a|^2+B|f_b|^2+2C|f_a||f_b|)dD. \tag{8}$$

$$Z_{v,x}=\frac{4\lambda^4}{\pi^4|K_w|^2}\int n(D)(B|f_a|^2+A|f_b|^2+2C|f_a||f_b|)dD. \tag{9}$$

Here, λ denotes the S-band radar wavelength, specifically 107 mm. The subscript x refers to rain, snow, or graupel. The dielectric factor for rainwater, $|Kw|^2$, is set to 0.93. The parameters A, B, and C in the equations are defined as functions of the mean canting angle (φ) and its associated standard deviation (σ), as expressed below:

$$\begin{aligned}
A&=\langle\cos^4\phi\rangle=\frac{1}{8}\left(3+4\cos2\bar{\phi}\,e^{-2\sigma^2}+\cos4\bar{\phi}\,e^{-8\sigma^2}\right),\\
B&=\langle\sin^4\phi\rangle=\frac{1}{8}\left(3-4\cos2\bar{\phi}\,e^{-2\sigma^2}+\cos4\bar{\phi}\,e^{-8\sigma^2}\right),\\
C&=\langle\sin^2\phi\cos^2\phi\rangle=\frac{1}{8}\left(1-\cos4\bar{\phi}\,e^{-8\sigma^2}\right).
\end{aligned} \tag{10}$$

f_a and f_b denote the backscattering amplitudes along the major and minor axes, respectively, and are expressed as power-law functions of the particle diameter D (mm).

$$\begin{aligned}
|f_a|&=\alpha_{xa}D^{\beta_{xa}},\\
|f_b|&=\alpha_{xb}D^{\beta_{xb}}.
\end{aligned} \tag{11}$$

The values of α_{xa}, α_{xb}, β_{xa}, and β_{xb} for pure rain, dry snow, and dry graupel are listed in Table 1. For wet snow and wet graupel, α_{xa}, α_{xb}, β_{xa}, and β_{xb} are expressed as polynomial functions of f_{wx},

$$\begin{aligned}
\alpha_{wxa}&=\sum_{k=0}^{\mathrm{n}}P_{wxak}f_{wx}^{k},\\
\alpha_{wxb}&=\sum_{k=0}^{n}P_{wxbk}f_{wx}^{k},
\end{aligned} \tag{12}$$

where the coefficients P_{wxak} and P_{wxbk} listed in Table 2, the value of n is 6 (Wang and Liu, 2019).

Table 1 Values of α_{xa}, α_{xb}, β_{xa}, and β_{xb}.

	α_{xa}	α_{xb}	β_{xa}	β_{xb}
rain	4.28×10^{-4}	4.28×10^{-4}	3.04	2.77

https://doi.org/10.5194/egusphere-2026-2230
Preprint. Discussion started: 27 July 2026

dry snow	0.194×10⁻⁴	0.191×10⁻⁴	3	3
dry graupel	0.105×10⁻³	0.092×10⁻³	3	3

Table 2 Values of P_{wxak} and P_{wxbk}

k	0	1	2	3	4	5	6
P_{wsak}	0.194×10^{-4}	7.094×10^{-4}	2.135×10^{-4}	-5.225×10^{-4}	0	0	0
P_{wgak}	0.191×10^{-3}	6.916×10^{-3}	-2.841×10^{-3}	-1.160×10^{-3}	0	0	0
P_{wsbk}	0.105×10^{-4}	1.821×10^{-4}	-3.765×10^{-4}	-0.797×10^{-4}	16.28×10^{-4}	-21.97×10^{-4}	8.744×10^{-4}
P_{wgbk}	0.092×10^{-3}	1.929×10^{-3}	-9.794×10^{-3}	29.24×10^{-3}	-48.19×10^{-3}	39.34×10^{-3}	-12.20×10^{-3}

2.1.2 Polarimetric radar operator with rain

By integrating the DSD in Eqs. (8) and (9), a simplified formula obtained for Z:

$$Z_{h,r}=\frac{4\lambda^4\alpha_{ra}^2N_{0r}}{\pi^4|K_w|^2}\Lambda_r^{-(2\beta_{ra}+1)}\Gamma(2\beta_{ra}+1), \tag{13}$$

$$Z_{v,r}=\frac{4\lambda^4\alpha_{rb}^2N_{0r}}{\pi^4|K_w|^2}\Lambda_r^{-(2\beta_{rb}+1)}\Gamma(2\beta_{rb}+1), \tag{14}$$

where, N_{0r} is the intercept parameter of the raindrop size distribution. N_{0r} is typically prescribed as a constant in single-moment microphysical schemes and does not vary with number concentration, with a value of 8×10^6 m⁻⁴. $\Gamma(\cdot)$ denotes the gamma function. The slope parameter of the rain distribution, Λ_r:

$$\Lambda_r=\left(\frac{\pi\rho_rN_{0r}}{\rho_aq_{pr}}\right)^{\frac{1}{4}}, \tag{15}$$

where, ρ_a is the air density. ρ_r denotes the density of rainwater, which is assumed to be constant and set to 1000 kg m⁻³. By substituting Eq. (15) into Eqs. (13) and (14) and simplifying the resulting expressions, obtain:

$$Z_{h,r}(q_{pr})=P_{h,r}(q_{pr})^{\frac{2\beta_{ra}+1}{4}}, \tag{16}$$

$$Z_{v,r}(q_{pr})=P_{v,r}(q_{pr})^{\frac{2\beta_{rb}+1}{4}}, \tag{17}$$

where, $P_{h/v,r}$:

$$P_{h,r}=\frac{4\lambda^4\alpha_{ra}^2}{\pi^4|K_w|^2}\left(\frac{\pi\rho_r}{\rho_a}\right)^{-\frac{2\beta_{ra}+1}{4}}(N_{0r})^{1-\frac{2\beta_{ra}+1}{4}}\Gamma(2\beta_{ra}+1), \tag{18}$$

https://doi.org/10.5194/egusphere-2026-2230
Preprint. Discussion started: 27 July 2026

$$P_{v,r} = \frac{4\lambda^4\alpha_{rb}^2}{\pi^4|K_w|^2}\left(\frac{\pi\rho_r}{\rho_a}\right)^{-\frac{2\beta_{rb}+1}{4}}(N_{0r})^{1-\frac{2\beta_{rb}+1}{4}}\Gamma(2\beta_{rb}+1). \tag{19}$$

$P_{h/v,r}$ is treated as a constant determined by the prescribed parameters in the formulation, and the values of α_{ra}, α_{rb}, β_{ra}, and β_{rb} are provided in Table 1.

2.1.3 Polarimetric radar operator with ice-phase

$Z_{h,x}$ and $Z_{v,x}$ denote the contributions of the ice-phase hydrometeors to the horizontal and vertical reflectivity, respectively.

$$Z_{h,x} = \frac{4\Gamma(2\beta_{xa}+1)\lambda^4 N_{0x}}{\pi^4|K_w|^2}\Lambda_x^{-(2\beta_{xa}+1)}(A\alpha_{xa}^2 + B\alpha_{xb}^2 + 2C\alpha_{xa}\alpha_{xb}), \tag{20}$$

$$Z_{v,x} = \frac{4\Gamma(2\beta_{xb}+1)\lambda^4 N_{0x}}{\pi^4|K_w|^2}\Lambda_x^{-(2\beta_{xb}+1)}(B\alpha_{xa}^2 + A\alpha_{xb}^2 + 2C\alpha_{xa}\alpha_{xb}), \tag{21}$$

where, x represents dry snow (ds), dry graupel (dg), wet snow (ws), and wet graupel (wg). N_{0x} is the intercept parameter for snow and graupel, with values of 3×10^6 and 4×10^5 m^{-4}, respectively. *A*, *B*, and *C* are defined as in Eq. (10). The values of α_{xa}, α_{xb}, β_{xa}, and β_{xb} for dry snow and dry graupel are given in Table 1, whereas those for wet snow and wet graupel are specified in Eq. (12). The slope parameters are given as follows:

$$\Lambda_x = \left(\frac{\pi\rho_x N_{0x}}{\rho_a q_x}\right)^{\frac{1}{4}}, \tag{22}$$

where ρ_x is the density of either snow (100 kg m^{-3}) or graupel (400 kg m^{-3}).

For dry snow and dry graupel, Eqs. (20) and (21) can be simplified to yield:

$$Z_{h,dx}(q_{dx}) = P_{h,dx}(q_{dx})^{\frac{2\beta_{dxa}+1}{4}}, \tag{23}$$

$$Z_{v,dx}(q_{dx}) = P_{v,dx}(q_{dx})^{\frac{2\beta_{dxb}+1}{4}}, \tag{24}$$

$$P_{h,dx} = \frac{4\Gamma(2\beta_{dxa}+1)\lambda^4 N_{0x}^{1-\frac{2\beta_{dxa}+1}{4}}}{\pi^4|K_w|^2}\left(\frac{\pi\rho_x}{\rho_a}\right)^{-\frac{2\beta_{dxa}+1}{4}}(A\alpha_{dxa}^2 + B\alpha_{dxb}^2 + 2C\alpha_{dxa}\alpha_{dxb}), \tag{25}$$

$$P_{v,dx} = \frac{4\Gamma(2\beta_{dxb}+1)\lambda^4 N_{0x}^{1-\frac{2\beta_{dxb}+1}{4}}}{\pi^4|K_w|^2}\left(\frac{\pi\rho_x}{\rho_a}\right)^{-\frac{2\beta_{dxb}+1}{4}}(B\alpha_{dxa}^2 + A\alpha_{dxb}^2 + 2C\alpha_{dxa}\alpha_{dxb}), \tag{26}$$

The contributions of wet snow and wet graupel to the horizontal and vertical reflectivity are given as follows:

$$Z_{h,wx}(q_{wx}, f_{wx}) = P_{h,wx} q_{wx}^{\frac{2\beta_{wxa}+1}{4}} \sum_{k=0}^{2n} P_{h,wxk} f_{wx}^k, \tag{27}$$

https://doi.org/10.5194/egusphere-2026-2230
Preprint. Discussion started: 27 July 2026

$$Z_{v,wx}(q_{wx}, f_{wx}) = P_{v,wx} q_{wx}^{\frac{2\beta_{wxb}+1}{4}} \sum_{k=0}^{2n} P_{v,wxk} f_{wx}^{k}, \tag{28}$$

where,

$$P_{h,wx} = \frac{4\Gamma(2\beta_{wxa}+1)\lambda^4 N_{0x}^{1-\frac{2\beta_{wxa}+1}{4}}}{\pi^4 |K_w|^2} \left(\frac{\pi\rho_x}{\rho_a}\right)^{-\frac{2\beta_{wxa}+1}{4}}, \tag{29}$$

$$P_{v,wx} = \frac{4\Gamma(2\beta_{wxb}+1)\lambda^4 N_{0x}^{1-\frac{2\beta_{wxb}+1}{4}}}{\pi^4 |K_w|^2} \left(\frac{\pi\rho_x}{\rho_a}\right)^{-\frac{2\beta_{wxb}+1}{4}}, \tag{30}$$

and,

$$P_{h,wxk} = AP_{Axk} + BP_{Bxk} + 2CP_{Cxk}, \tag{31}$$

$$P_{v,wxk} = BP_{Axk} + AP_{Bxk} + 2CP_{Cxk}, \tag{32}$$

$$\begin{aligned}
P_{Axk} &= \begin{cases} \sum_{i=0}^{k} P_{wxai} P_{wxa(k-i)}, (k \le n) \\ \sum_{i=k-n}^{n} P_{wxai} P_{wxa(k-i)}, (k > n) \end{cases} \\
P_{Bxk} &= \begin{cases} \sum_{i=0}^{k} P_{wxbi} P_{wxb(k-i)}, (k \le n) \\ \sum_{i=k-n}^{n} P_{wxbi} P_{wxb(k-i)}, (k > n) \end{cases} \\
P_{Cxk} &= \begin{cases} \sum_{i=0}^{k} P_{wxai} P_{wxb(k-i)}, (k \le n) \\ \sum_{i=k-n}^{n} P_{wxai} P_{wxb(k-i)}, (k > n) \end{cases}
\end{aligned} \tag{33}$$

where, P_{wxa} and P_{wxb} are constants, with their values given in Table 2. A detailed derivation of Eq. (33) can be found in Wang and Zhang (2019).

2.2 Tangent-linear and adjoint operators with ice-phase for dual-polarization radar observations (RadDualIceVar)

For the TL and AD operator, the formulation for vertical reflectivity is supplemented following Wang and Liu (2018), and the complete expressions are listed below. In RadDualIceVar, Zdr is incorporated into the assimilation through Eq. (7) using the vertical reflectivity and is updated iteratively.

$$\begin{aligned}
\delta Z_{h,r}(q_{pr}) &= \frac{\partial Z_{h,r}(q_{pr})}{\partial q_{pr}} \frac{\partial q_{pr}}{\partial q_r} \delta q_r \\
&= \frac{2\beta_{ra}+1}{4} P_{h,r} (q_{pr})^{\frac{2\beta_{ra}+1}{4}-1} (1 - F_{ws} - F_{wg}) \delta q_r,
\end{aligned} \tag{34}$$

$$\begin{aligned}
\delta Z_{v,r}(q_{pr}) &= \frac{\partial Z_{v,r}(q_{pr})}{\partial q_{pr}} \frac{\partial q_{pr}}{\partial q_r} \delta q_r \\
&= \frac{2\beta_{rb}+1}{4} P_{v,r} (q_{pr})^{\frac{2\beta_{rb}+1}{4}-1} (1 - F_{ws} - F_{wg}) \delta q_r,
\end{aligned} \tag{35}$$

https://doi.org/10.5194/egusphere-2026-2230
Preprint. Discussion started: 27 July 2026

$$\begin{aligned}\delta Z_{h,dx}(q_{dx}) &= \frac{\partial Z_{h,dx}(q_{dx})}{\partial q_{dx}}\frac{\partial q_{dx}}{\partial q_x}\delta q_x \\ &= \frac{2\beta_{dxa}+1}{4}P_{h,dx}(q_{dx})^{\frac{2\beta_{dxa}+1}{4}-1}(1-F_{wx})\delta q_x,\end{aligned} \tag{36}$$

$$\begin{aligned}\delta Z_{v,dx}(q_{dx}) &= \frac{\partial Z_{v,dx}(q_{dx})}{\partial q_{dx}}\frac{\partial q_{dx}}{\partial q_x}\delta q_x \\ &= \frac{2\beta_{dxb}+1}{4}P_{v,dx}(q_{dx})^{\frac{2\beta_{dxb}+1}{4}-1}(1-F_{wx})\delta q_x,\end{aligned} \tag{37}$$

$$\begin{aligned}\delta Z_{h,wx}(q_{wx},f_{wx}) &= \frac{\partial Z_{h,wx}}{\partial q_{wx}}\left(\frac{\partial q_{wx}}{\partial q_x}\delta q_x+\frac{\partial q_{wx}}{\partial q_r}\delta q_r\right)+\frac{\partial Z_{h,wx}}{\partial f_{wx}}\left(\frac{\partial f_{wx}}{\partial q_x}\delta q_x+\frac{\partial f_{wx}}{\partial q_r}\delta q_r\right) \\ &= \left(\frac{\partial Z_{h,wx}}{\partial q_{wx}}\frac{\partial q_{wx}}{\partial q_r}+\frac{\partial Z_{h,wx}}{\partial f_{wx}}\frac{\partial f_{wx}}{\partial q_r}\right)\delta q_r+\left(\frac{\partial Z_{h,wx}}{\partial q_{wx}}\frac{\partial q_{wx}}{\partial q_x}+\frac{\partial Z_{h,wx}}{\partial f_x}\frac{\partial f_{wx}}{\partial q_r}\right)\delta q_x \\ &= \Big\{\frac{2\beta_{wxa}+1}{4}P_{h,wx}q_{wx}^{\frac{2\beta_{dxa}+1}{4}-1}F_{wx}\left(\sum_{k=0}^{2n}P_{h,wxk}f_{wx}^k\right) \\ &\quad +P_{h,wx}q_{wx}^{\frac{2\beta_{wxa}+1}{4}}\left[\sum_{k=0}^{2n}P_{h,wxk}kf_{wx}^k\left(\frac{1}{q_r}-\frac{1}{q_r+q_x}\right)\right]\Big\}\delta q_r \\ &\quad +\Big\{\frac{2\beta_{wxa}+1}{4}P_{h,wx}q_{wx}^{\frac{2\beta_{dxa}+1}{4}-1}F_{wx}\left(\sum_{k=0}^{2n}P_{h,wxk}f_{wx}^k\right) \\ &\quad +P_{h,wx}q_{wx}^{\frac{2\beta_{wxa}+1}{4}}\left[\sum_{k=0}^{2n}P_{h,wxk}kf_{wx}^k\left(-\frac{1}{q_r+q_x}\right)\right]\Big\}\delta q_x,\end{aligned} \tag{38}$$

$$\begin{aligned}\delta Z_{v,wx}(q_{wx},f_{wx}) &= \frac{\partial Z_{v,wx}}{\partial q_{wx}}\left(\frac{\partial q_{wx}}{\partial q_x}\delta q_x+\frac{\partial q_{wx}}{\partial q_r}\delta q_r\right)+\frac{\partial Z_{v,wx}}{\partial f_{wx}}\left(\frac{\partial f_{wx}}{\partial q_x}\delta q_x+\frac{\partial f_{wx}}{\partial q_r}\delta q_r\right) \\ &= \left(\frac{\partial Z_{v,wx}}{\partial q_{wx}}\frac{\partial q_{wx}}{\partial q_r}+\frac{\partial Z_{v,wx}}{\partial f_{wx}}\frac{\partial f_{wx}}{\partial q_r}\right)\delta q_r+\left(\frac{\partial Z_{v,wx}}{\partial q_{wx}}\frac{\partial q_{wx}}{\partial q_x}+\frac{\partial Z_{v,wx}}{\partial f_x}\frac{\partial f_{wx}}{\partial q_r}\right)\delta q_x \\ &= \Big\{\frac{2\beta_{wxb}+1}{4}P_{v,wx}q_{wx}^{\frac{2\beta_{wxb}+1}{4}-1}F_{wx}\left(\sum_{k=0}^{2n}P_{v,wxk}f_{wx}^k\right) \\ &\quad +P_{v,wx}q_{wx}^{\frac{2\beta_{wxb}+1}{4}}\left[\sum_{k=0}^{2n}P_{v,wxk}kf_{wx}^k\left(\frac{1}{q_r}-\frac{1}{q_r+q_x}\right)\right]\Big\}\delta q_r \\ &\quad +\Big\{\frac{2\beta_{wxb}+1}{4}P_{v,wx}q_{wx}^{\frac{2\beta_{wxb}+1}{4}-1}F_{wx}\left(\sum_{k=0}^{2n}P_{v,wxk}f_{wx}^k\right) \\ &\quad +P_{v,wx}q_{wx}^{\frac{2\beta_{wxb}+1}{4}}\left[\sum_{k=0}^{2n}P_{v,wxk}kf_{wx}^k\left(-\frac{1}{q_r+q_x}\right)\right]\Big\}\delta q_x,\end{aligned} \tag{39}$$

$$\delta Z_{H/V}=10\cdot\frac{1}{Z_{h/v}\ln 10}\delta Z_{h/v}. \tag{40}$$

The AD operator is defined as the transpose of the TL operator. Consequently, the adjoint formulations for horizontal and

https://doi.org/10.5194/egusphere-2026-2230
Preprint. Discussion started: 27 July 2026

vertical reflectivity can be expressed as follows:

$$\delta Z_{h/v}^{A} = 10 \cdot \frac{1}{Z_{h/v} \ln 10} \delta Z_{H/V}, \tag{41}$$

Here, the superscript "A" denotes the AD operator. The AD variables δq_r^A and δq_x^A correspond to rainwater and ice-phase hydrometeors, respectively. Owing to the structure of the TL operator, in which both horizontal and vertical reflectivity depend on the contributions from rain and ice-phase hydrometeors, the corresponding AD operators are jointly influenced by the horizontal and vertical reflectivity components.

$$\begin{aligned} \delta q_r^A &= \delta q_r^A + \frac{2\beta_{ra}+1}{4} P_{h,r}(q_{pr})^{\frac{2\beta_{ra}+1}{4}-1}(1-F_{ws}-F_{wg})\delta Z_h^A \\ &+ \frac{2\beta_{rb}+1}{4} P_{v,r}(q_{pr})^{\frac{2\beta_{rb}+1}{4}-1}(1-F_{ws}-F_{wg})\delta Z_v^A, \end{aligned} \tag{42}$$

$$\begin{aligned} \delta q_x^A &= \delta q_x^A + \frac{2\beta_{dxa}+1}{4} P_{h,dx}(q_{dx})^{\frac{2\beta_{dxa}+1}{4}-1}(1-F_{wx})\delta Z_h^A \\ &+ \frac{2\beta_{dxb}+1}{4} P_{v,dx}(q_{dx})^{\frac{2\beta_{dxb}+1}{4}-1}(1-F_{wx})\delta Z_v^A, \end{aligned} \tag{43}$$

$$\begin{aligned} \delta q_r^A &= \delta q_r^A + \frac{2\beta_{wxa}+1}{4} P_{h,wx}(q_{wx})^{\frac{2\beta_{wxa}+1}{4}-1} F_{wx}\left(\sum_{k=0}^{2n} P_{h,wxk} f_{wx}^k\right)\delta Z_h^A \\ &+ P_{h,wx} q_{wx}^{\frac{2\beta_{wxa}+1}{4}}\left[\sum_{k=0}^{2n} P_{h,wxk} k f_{wx}^k \left(\frac{1}{q_r} - \frac{1}{q_r+q_x}\right)\right]\delta Z_h^A \\ &+ \delta q_r^A + \frac{2\beta_{wxb}+1}{4} P_{v,wx}(q_{wx})^{\frac{2\beta_{wxb}+1}{4}-1} F_{wx}\left(\sum_{k=0}^{2n} P_{v,wxk} f_{wx}^k\right)\delta Z_v^A \\ &+ P_{v,wx} q_{wx}^{\frac{2\beta_{wxb}+1}{4}}\left[\sum_{k=0}^{2n} P_{v,wxk} k f_{wx}^k \left(\frac{1}{q_r} - \frac{1}{q_r+q_x}\right)\right]\delta Z_v^A, \end{aligned} \tag{44}$$

$$\begin{aligned} \delta q_x^A &= \delta q_x^A + \frac{2\beta_{wxa}+1}{4} P_{h,wx}(q_{wx})^{\frac{2\beta_{wxa}+1}{4}-1} F_{wx}\left(\sum_{k=0}^{2n} P_{h,wxk} f_{wx}^k\right)\delta Z_h^A \\ &+ P_{h,wx} q_{wx}^{\frac{2\beta_{wxa}+1}{4}}\left[\sum_{k=0}^{2n} P_{h,wxk} k f_{wx}^k \left(-\frac{1}{q_r+q_x}\right)\right]\delta Z_h^A \\ &+ \delta q_x^A + \frac{2\beta_{wxb}+1}{4} P_{v,wx}(q_{wx})^{\frac{2\beta_{wxb}+1}{4}-1} F_{wx}\left(\sum_{k=0}^{2n} P_{v,wxk} f_{wx}^k\right)\delta Z_v^A \\ &+ P_{v,wx} q_{wx}^{\frac{2\beta_{wxb}+1}{4}}\left[\sum_{k=0}^{2n} P_{v,wxk} k f_{wx}^k \left(-\frac{1}{q_r+q_x}\right)\right]\delta Z_v^A, \end{aligned} \tag{45}$$

2.3 Validation of RadDualIceVar

To verify the correctness of the TL implementation, the TL operator is tested using the following relation:

https://doi.org/10.5194/egusphere-2026-2230
Preprint. Discussion started: 27 July 2026

$$\frac{\left|H(\mathbf{x}+\alpha\delta\mathbf{x})-H(\mathbf{x})\right|}{|\alpha|\left|\mathbf{H}\delta\mathbf{x}\right|}=1+O(\alpha), \tag{46}$$

where H denotes the nonlinear observation operator, and $\mathbf{H}$ represents its TL operator. A ratio approaching unity indicates the numerical consistency of the TL operator. Here, α is a perturbation scaling factor applied to q_r, q_s, and q_g, and the resulting perturbations are shown below.

In the study of Wang and Liu (2018), several variables were treated as constants in the construction of the TL operator, and it was shown that this simplification does not significantly degrade assimilation performance. In the present study, a similar TL test is first conducted following their implementation, yielding comparable results, with test accuracy ranging from 10^{-2} to 10^{-4}.

When F in Eq. (1) is treated as a variable in the TL operator, the test accuracy can reach machine precision, provided that the evaluation point is sufficiently far from the discontinuities in Eq. (1). To further evaluate the intrinsic performance of the TL operator under different microphysical regimes, single-observation tests are conducted with F treated as a variable at three representative altitudes (1.5, 5, and 9 km), corresponding primarily to rain-dominated, mixed-phase, and ice-phase conditions, respectively. The test results indicate that the TL operator exhibits high fidelity in both the pure-rain and ice-phase regimes, with the consistency ratio remaining close to 1. In contrast, numerical accuracy diminishes within the mixed-phase regime. This reduced performance is likely due to the increased complexity and nonlinearity of the operator. However, due to the non-smoothness of Eq. (1), assimilation experiments indicate that treating F as a constant leads to better convergence for a fixed number of iterations. Therefore, F is treated as a constant in the TL operator in the subsequent experiments.

Table 3 Results of the TL test at different altitudes

α	RF			RFV		
	1.5km	5km	9km	1.5km	5km	9km
10^{-1}	0.999518133274039	1.00400367789455	0.999525654708671	0.999518133273986	1.00252581335674	0.999525654715028
10^{-2}	0.999951785444071	1.00285606945050	0.999956037331048	0.999951785450927	1.00139542426461	0.999956037345221
10^{-3}	0.999995178261278	1.00274137608492	0.999999102762139	0.999995178274462	1.00128243889122	0.999999102766545
10^{-4}	0.999999517445276	1.00272990672217	1.00000340950352	0.999999517084902	1.00127114041196	1.00000340950792
10^{-5}	0.999999945701496	1.00272875752419	1.00000384120319	0.999999950623678	1.00127000776959	1.00000384120759
10^{-6}	0.999999926540144	1.00272851647751	1.00000386073711	0.999999919508455	1.00126977692900	1.00000386074151
10^{-7}	1.00000030976719	1.00272773771053	1.00000298171063	0.999999712073634	1.00126918748862	1.00000395841112
10^{-8}	0.999992645226332	1.00273727676952	1.00000005162238	0.999991414680782	1.00126440253068	1.00000005162679
10^{-9}	1.00003096793060	1.00271819539274	1.00003911946571	0.999939555975463	1.00126440237638	0.999941449861804
10^{-10}	0.999264513845199	1.00176413429693	0.999160092990935	0.998798664458428	1.00069039257553	1.00013678907842
10^{-11}	0.996390311024935	1.00176413429538	0.996230004741694	0.995687142139243	1.00451712447676	0.996230004746084
10^{-12}	0.958067606754745	0.954061080281171	0.976696083080092	0.933456695755540	0.956682975692002	0.976696083084396

The model AD operator is tested using the adjoint test in WRFDA. If the adjoint is correctly implemented, the inner products

https://doi.org/10.5194/egusphere-2026-2230
Preprint. Discussion started: 27 July 2026

on both sides should be nearly identical.

$$\left\langle \mathbf{H}\delta x, \delta y \right\rangle = \left\langle \delta x, \mathbf{H}^{*}\delta y \right\rangle, \tag{47}$$

In this study, we selected a point near the melting layer (5015.6 m) where hydrometeors of different phases coexist for verification. The inner products on both sides of the adjoint test were found to be 1.10628701089485 × 10^{-2}, achieving a precision of 10^{-16}, successfully passing the adjoint test.

The gradient of the operator is tested following the WRFDA gradient-checking procedure.

$$\begin{aligned} &T(\alpha) = \frac{f(x+\alpha h) - f(x)}{\alpha \nabla f(x) \cdot h}, \\ &h = -\nabla f(x), \\ &\lim_{\alpha \to 0} T(\alpha) = 1. \end{aligned} \tag{48}$$

Here, $f(x)$ denotes the cost function, α is a small perturbation magnitude, and h represents the perturbation direction. A perturbation is applied at the point x along the direction h. If the gradient is computed correctly, T should approach 1.

Table 4 Results of gradient test

α	T
10^{-10}	1.00024201343447
10^{-9}	1.00001375912415
10^{-8}	1.00000612773004
10^{-7}	1.00000007466931
10^{-6}	0.999999527114324
10^{-5}	0.999995000135980
10^{-4}	0.999950000551035
10^{-3}	0.999500000005679

3 Experimental Design and Data

To evaluate the performance of RadDualIceVar, a real-case experiment is conducted using Typhoon Doksuri (2023) as the test case to assess the impact of incorporating the Zdr variable on the analysis and subsequent forecasts. Typhoon Doksuri was an intense tropical cyclone that occurred in 2023, with a peak maximum wind speed reaching 62 m s^{-1}. After its formation on 21 July, Doksuri rapidly intensified into a super typhoon by 24 July. It made landfall over Jinjiang City, Fujian Province, on 28 July at the typhoon intensity, bringing severe rainfall and strong winds to the affected regions. Following landfall, the remnant circulation of Doksuri persisted and penetrated far inland over northern China, leading to prolonged and heavy

https://doi.org/10.5194/egusphere-2026-2230
Preprint. Discussion started: 27 July 2026

precipitation over large areas of northern China.

Three numerical experiments are designed (Table 5): a control experiment without radar data assimilation (CTRL), an experiment assimilating radar reflectivity and radial velocity (RF), and an experiment assimilating radar reflectivity, radial velocity, and Zdr (RFZDR). The overall data assimilation framework is illustrated in Fig. 1. A 6-h spin-up integration is first performed from 1200 UTC to 1800 UTC to allow the model to dynamically adjust. This is followed by a 6-h cycling data assimilation period with a 30-min assimilation interval. Subsequently, a 6-h deterministic forecast is initialized at 0000 UTC on 28 July.

Table 5 Experimental Design

	Assimilated data
CTRL	No DA
RF	RV+RF
RFZDR	RV+RF+ZDR

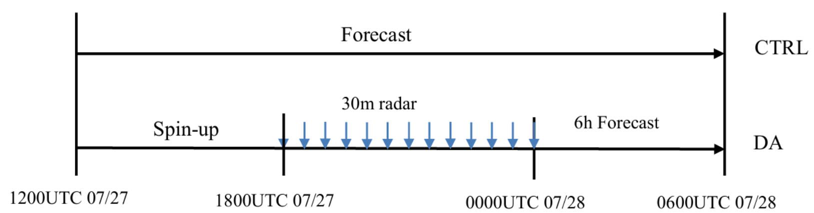

Figure 1 Flowchart of the experiments

All experiments are conducted in the framework of the WRF Model, version 4.1. The NCEP FNL dataset was used as the initial and lateral boundary conditions in this study. The model domain consists of a single domain with 601 × 601 horizontal grid points at a grid spacing of 5 km, and 41 vertical levels extending up to a model top of 10 hPa. The Thompson microphysics scheme (Thompson et al., 2004) is employed. The Rapid Radiative Transfer Model for General Circulation Models (RRTMG) Shortwave and Longwave Schemes (Iacono et al., 2008) are used for radiation. The Revised MM5 Scheme (Jimenez et al., 2012) is selected for the surface layer options, and the Unified Noah Land Surface Model (Tewari et al., 2004) is used for the land surface options. The Yonsei University Scheme (YSU) (Hou et al., 2006) is applied for the planetary boundary layer physics, and the Kain–Fritsch Scheme (Kain, 2004) is adopted for cumulus parameterization. Adjusting the length scale of the background error covariance can enhance small- and medium-scale weather features (Ha and Lee, 2012; Shen and Min, 2015). In this study, a length-scale factor of 0.3 is adopted for the assimilation of dual-polarization radar data.

The background error covariance matrix is constructed utilizing the GEN_BE system (Descombes et al., 2015). The

https://doi.org/10.5194/egusphere-2026-2230
Preprint. Discussion started: 27 July 2026

resulting dataset includes hydrometeor mixing ratios for rainwater (qr), snow (qs), and graupel (qg). Following the National Meteorological Center (NMC) method (Parrish and Derber, 1992), the covariance is estimated from forecast differences. In this study, a set of 20 days of forecasts covering the period from 10 to 29 July 2023 is initialized from the NCEP FNL dataset to derive the background error statistics.

Observations from an integrated network of three S-band Doppler radars (located at Quanzhou, Xiamen, and Shantou) were utilized in this study. To ensure the fidelity of the variables, quality control procedures were applied prior to data assimilation. These steps include Doppler velocity dealiasing and ground clutter removal. In this study, the UNRAVEL algorithm was employed to perform preliminary velocity folding processing in the radar radial wind data (Louf et al., 2020). In this study, the observation errors for horizontal reflectivity and radial velocity are specified as 5 dBZ and 2 m s^{-1}, respectively. When Zdr is assimilated, an iterative analysis is performed following the vertical reflectivity, and the observation error of the vertical reflectivity is set to 5 dBZ.

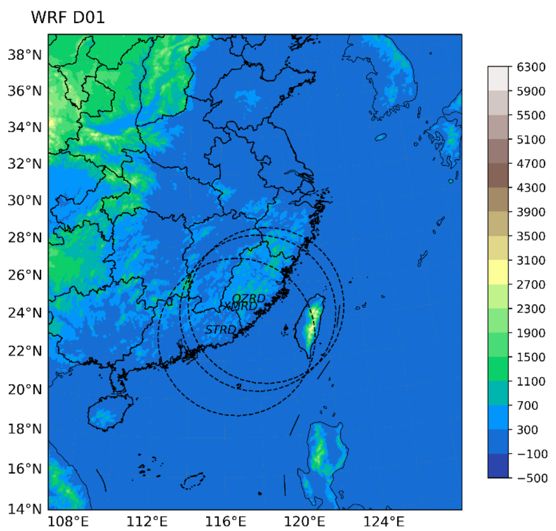

Figure 2 Model domain and radar stations for the typhoon case. Circles indicate the coverage of the radars. QZRD, XMRD, and STRD represent radars from the cities of Quanzhou, Xiamen, and Shantou city, respectively

4 Results

4.1 Single observation test

To assess the physical consistency of the analysis increments generated through the direct assimilation of dual-polarization radar observations. Two single-observation tests were compared: one assimilating horizontal reflectivity alone (RF) and another incorporating both reflectivity and differential reflectivity (RFZDR). The single observation is located at 24.220°N, 118.749°E and a model height of 5015.6 m, with the horizontal reflectivity factor specified as 36.562 dBZ and the

https://doi.org/10.5194/egusphere-2026-2230
Preprint. Discussion started: 27 July 2026

differential reflectivity prescribed as 0.595 dB.

Figure 3 presents the horizontal distributions of hydrometeor analysis increments at selected model levels for the RF and RFZDR experiments. The first row shows the increments obtained from the RF experiment, while the second row corresponds to the RFZDR experiment. In both experiments, negative increments are produced for all hydrometeor species shown, indicating a reduction of hydrometeor mixing ratios in response to the assimilated observation, as the background values exceed the prescribed observation.

Notable differences are evident between the two experiments. In the RF assimilation, the analysis increments remain relatively weak and spatially confined across rainwater, graupel, and snow. In contrast, when Zdr is additionally assimilated, the magnitude of the negative increments is enhanced, and the affected area becomes more spatially extensive, particularly for graupel and snow at 500 hPa. This behavior suggests that the inclusion of Zdr introduces additional microphysical constraints that more strongly modulate the ice-phase hydrometeor, while maintaining a coherent horizontal response centered on the observation location.

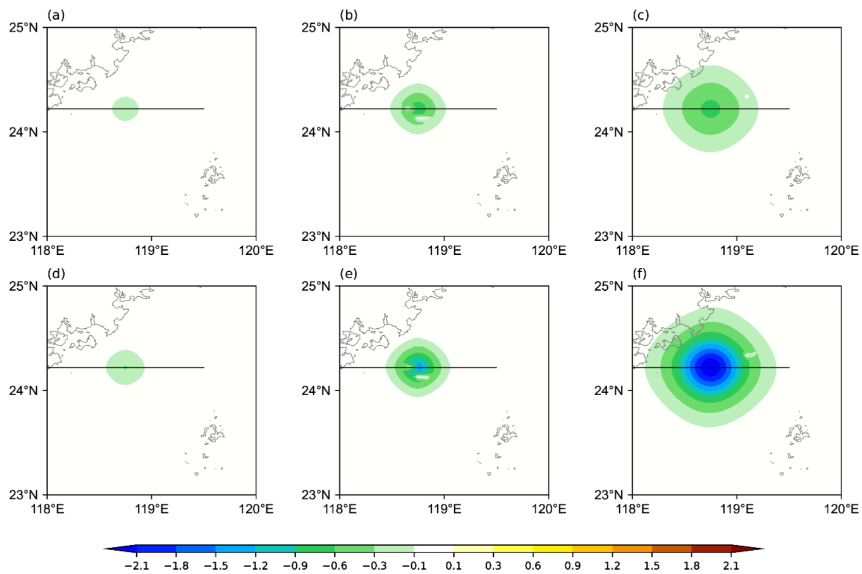

Figure 3 Single-observation hydrometeor analysis increments from the RF experiment (the first row) and the RFZDR experiment (the second row) for qr (the first column) at 850 hPa (units: 10^{-1} g kg^{-1}), qg (the second column) at 500 hPa (units: 10^{-5} g kg^{-1}), and qs (the third column) at 500 hPa (units: 10^{-3} g kg^{-1}).

Figure 4 illustrates the vertical cross sections of the hydrometeor analysis increments along the transect denoted by the black line in Fig. 3 for both RF and RFZDR single-observation tests. In both experiments, the vertical distributions of the analysis increments exhibit a clear phase-dependent structure. Changes in rainwater mixing ratio are primarily confined below

https://doi.org/10.5194/egusphere-2026-2230
Preprint. Discussion started: 27 July 2026

the melting layer, whereas graupel increments are concentrated in the vicinity of the melting layer. Snow mixing ratio increments are mainly distributed above the melting layer, extending into the upper-level region. This vertically stratified pattern indicates that the assimilated observational information is projected onto the model hydrometeor in a physically consistent manner and conforms to the phase-dependent constraints imposed by the observation operator.

Relative to the RF experiment, the RFZDR experiment produces larger-magnitude extrema in hydrometeor mixing ratio increments throughout the vertical column. In particular, the extrema of the snow mixing ratio reach approximately -2.1×10^{-3} g kg^{-1}, while the rainwater mixing ratio exhibits extrema of about -0.6×10^{-1} g kg^{-1}. In addition, the graupel in the RFZDR experiment shows a broader vertical and horizontal extent of significant increments, especially near the melting layer. These results indicate that, compared with reflectivity-only assimilation, the inclusion of Zdr leads to stronger adjustments of hydrometeors.

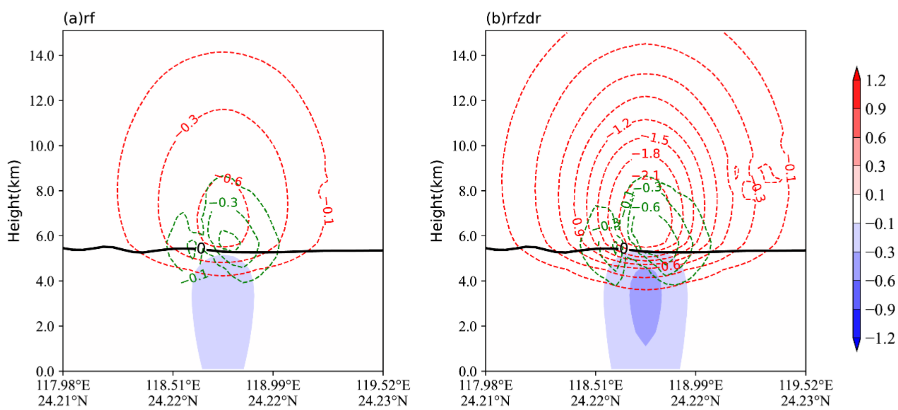

Figure 4 Vertical cross sections of single-observation hydrometeor analysis increments from (a) the RF experiment and (b) the RFZDR experiment. Shading indicates qr (units: 10^{-1} g kg^{-1}), green contours denote qg (units: 10^{-5} g kg^{-1}), and red contours denote qs (units: 10^{-3} g kg^{-1}).

4.2 Real data assimilation experiments

4.2.1 Evaluation of analyses

Figure 5 depicts the horizontal composite reflectivity of Typhoon Doksuri at the onset (1800 UTC 27 July) and at the end (0000 UTC 28 July) of the data assimilation period. The upper and lower panels correspond to the initial and final assimilation cycles, respectively.

At 1800 UTC (Fig. 5a), the observed composite reflectivity shows a well-organized tropical cyclone structure, characterized by a distinct inner-core region and pronounced spiral rainbands. Intense convective echoes exceeding 40 dBZ are primarily distributed along the outer spiral rainbands and in the vicinity of the eyewall.

Relative to the CTRL experiment (Fig. 5b), the assimilation leads to a pronounced improvement in the simulated

https://doi.org/10.5194/egusphere-2026-2230
Preprint. Discussion started: 27 July 2026

reflectivity structure. Both the RF and RFZDR experiments (Figs. 5c and 5d) exhibit a noticeable reduction of excessively strong near-coastal echoes and a closer correspondence to the observed reflectivity pattern within the black box shown in Fig. 5a. In addition, relative to the RF experiment, the RFZDR experiment produces a more continuous and spatially coherent distribution of reflectivity exceeding 40 dBZ in the inner-core and rainband regions, suggesting a stronger constraint on convective-scale precipitation structures when Zdr is included.

At the final assimilation time (Figs. 5e–h), further differences among the experiments become evident. The assimilation of radar observations significantly improves the typhoon representation, with the simulated centers in both the RF and RFZDR experiments showing closer agreement with the observed position. In contrast, the CTRL experiment exhibits a pronounced westward displacement of the cyclonic center relative to the observations. Despite this improvement in storm positioning, both radar-assimilated experiments still produce stronger composite reflectivity in the spiral rainbands near the typhoon center compared with the observations. Nevertheless, the RFZDR experiment shows a reflectivity distribution that is more consistent with the observed rainband structure than that of the RF experiment.

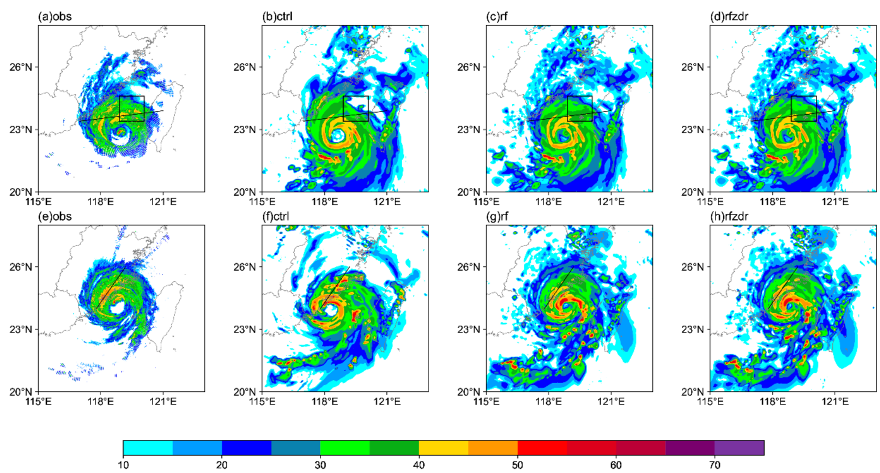

Figure 5 Composite reflectivity. The first row corresponds to the first assimilation time, and the second row corresponds to the final assimilation time. Panels (a, e) show observations, panels (b, f) show the CTRL experiment, panels (c, g) show the RF experiment, and panels (d, h) show the RFZDR experiment.

Figure 6 shows vertical cross sections of composite reflectivity along the black line indicated in Fig. 5 for the observations and the CTRL, RF, and RFZDR experiments. In the observations, reflectivity is primarily confined below approximately 6 km, with limited echo intensity aloft. In contrast, the CTRL experiment produces pronounced reflectivity exceeding 30 dBZ above 6 km, indicating the presence of spurious high-level echoes in the simulated storm structure. These unrealistically strong echoes at upper levels are effectively suppressed in both the RF and RFZDR experiments after radar data assimilation. This result

https://doi.org/10.5194/egusphere-2026-2230
Preprint. Discussion started: 27 July 2026

suggests that the radar observation operator imposes physically reasonable vertical constraints on the analyzed reflectivity, particularly by limiting excessive ice-phase contributions at upper levels.

At the initial assimilation time, differences between the two radar-assimilated experiments become evident. Compared with the RF experiment, RFZDR more accurately reproduces the observed vertical structure of intense echoes, including the three distinct regions with reflectivity exceeding 40 dBZ. At the final assimilation time, the RFZDR experiment, compared with the RF experiment, simulates a strong reflectivity core exceeding 40 dBZ that is close to the observations, albeit with a slight positional offset.

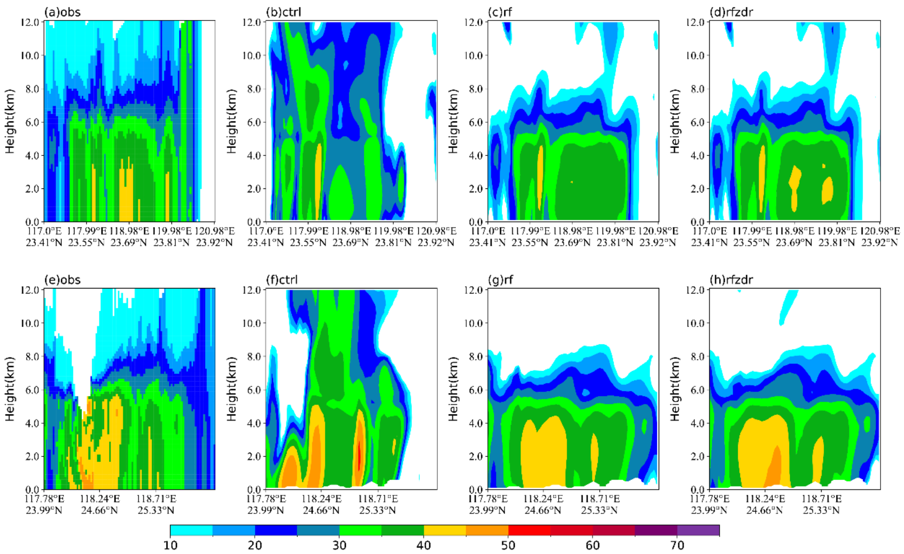

Figure 6 Vertical cross sections of reflectivity. The first row corresponds to the first assimilation time, and the second row corresponds to the final assimilation time. Panels (a, e) show observations, panels (b, f) show the CTRL experiment, panels (c, g) show the RF experiment, and panels (d, h) show the RFZDR experiment.

Contoured Frequency by Altitude Diagrams (CFADs) are utilized to characterize the vertical statistical distributions of reflectivity, providing insight into the impact of radar data assimilation on the simulated hydrometeor structures. Figure 7 illustrates the CFADs of reflectivity at the final assimilation cycle for Region A (as defined in Fig. 5). The horizontal black line in Fig. 6 denotes the 0°C level at an altitude of approximately 6 km. In the observations, reflectivity above the melting layer is predominantly distributed below 25 dBZ, indicating relatively weak radar returns associated with ice-phase hydrometeors. Below the melting layer, reflectivity values are mainly concentrated between 20 and 45 dBZ, reflecting the presence of rain-phase precipitation and melting particles. This vertical contrast highlights the strong phase dependence of the observed reflectivity distribution.

The CTRL experiment (Fig. 7b) exhibits a markedly different vertical distribution. Similar to the vertical cross sections

https://doi.org/10.5194/egusphere-2026-2230
Preprint. Discussion started: 27 July 2026

shown in Figs. 6b and 6f, reflectivity exceeding 30 dBZ occurs frequently above 6 km, suggesting an overestimation of ice-phase scattering contributions and the presence of unrealistically strong high-level echoes. Such a bias indicates deficiencies in the background hydrometeor representation in the absence of radar data assimilation. The assimilation experiments substantially alleviate this issue. In both the RF and RFZDR experiments, the frequency of strong reflectivity above the melting layer is reduced, indicating that the radar observation operator effectively constrains the vertical distribution of reflectivity and suppresses excessive high-level echoes. Nevertheless, reflectivity exceeding 30 dBZ still appears at upper levels in the RF experiment, implying that reflectivity-only assimilation provides limited constraints on ice-phase hydrometeor properties.

In comparison, the RFZDR experiment exhibits a more realistic vertical reflectivity distribution above the melting layer. The frequency of high-level reflectivity is further reduced, and the overall distribution is shifted toward weaker values, which is more consistent with the observations. This improvement can be attributed to the additional microphysical information provided by Zdr, which enhances the sensitivity of the observation operator to ice-phase hydrometeors, particularly snow, and imposes stronger constraints on their vertical distribution. Near the melting layer (4–6 km), the CFAD in the RFZDR experiment shows a closer agreement with the observed frequency distribution, with a partial suppression of reflectivity exceeding 40 dBZ. This result suggests that the inclusion of Zdr helps to moderate excessive reflectivity associated with mixed-phase processes and contributes to a more physically consistent transition across the melting layer.

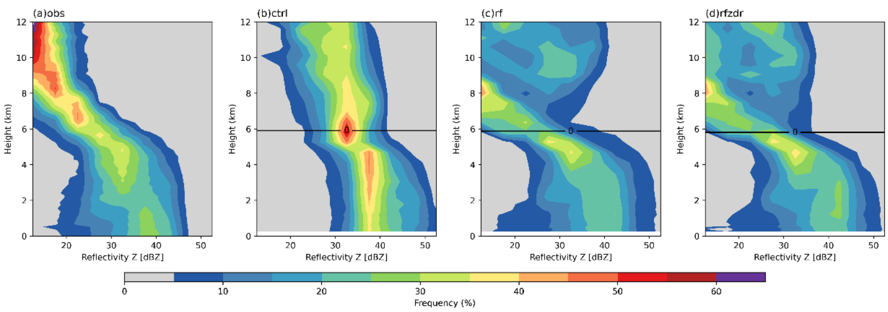

Figure 7 CFAD of reflectivity at the final assimilation time for region A shown in Fig. 5.

The horizontal distribution of Zdr at 2 km altitude at 0000 UTC on 28 July is shown in Fig. 8 for the observations and the CTRL, RF, and RFZDR experiments.

Regions of high Zdr are primarily located within the eyewall and spiral rainbands of the typhoon, where values generally exceed 1 dB and can reach above 2 dB in the eyewall region (Fig. 8a). Compared to the CTRL experiment, the RF and RFZDR experiments show improved skill in reproducing the spatial distribution of Zdr. This improvement is consistent with the patterns shown in Fig. 5(g–h). However, compared with the observations, the simulated Zdr values are consistently overestimated in all experiments. This trend is broadly consistent with previous studies. In rain-dominated regions, the simulated Zdr is systematically higher than observations. This positive bias is evident across different forward operators,

https://doi.org/10.5194/egusphere-2026-2230
Preprint. Discussion started: 27 July 2026

including those based on the T-matrix method (Jung et al., 2008), direct assimilation using warm-rain schemes (Kawabata et al., 2018), and simplified formulations that relate water content to the mass-weighted mean diameter of hydrometeors (Zhang et al., 2021). Liu et al. (2024b) modified the melting-layer parameterization in the operator, which leads to a reduction in Zdr compared with the earlier scheme.

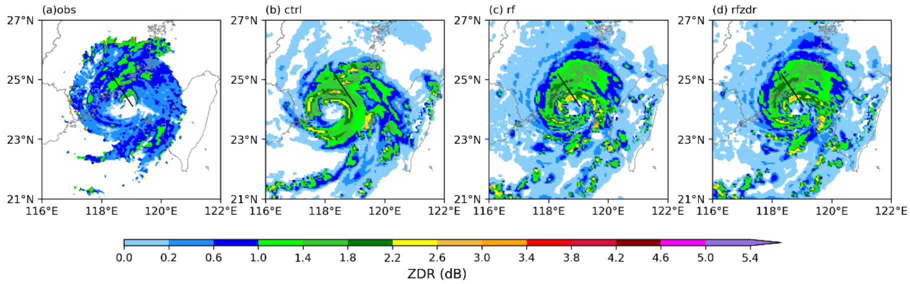

Figure 8 Horizontal distribution of Zdr at 2 km altitude at the final assimilation time, (a) observations, simulated with (b) CTRL, (c) RF, and (d) RFZDR.

Fig. 9 presents the vertical cross section along the black line in Fig. 8. The observed Zdr exhibits pronounced high-value regions in regions A and B, while the simulated Zdr is primarily confined below 6 km. In the eyewall region (region B), Zdr values exceeding 2 dB are evident and are well reproduced in both the RF and RFZDR experiments. In the spiral rainband region (region A), the observed Zdr ranges from 1 to 2.2 dB. The assimilation experiments capture the location of the high-Zdr region reasonably well, although the simulated values are slightly higher than the observations.

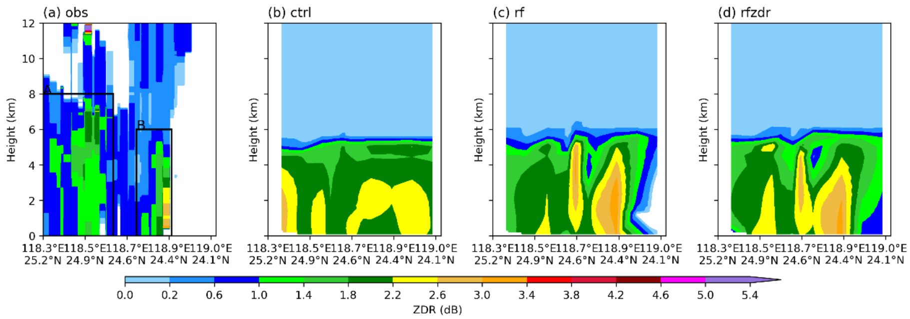

Figure 9 Vertical cross sections of reflectivity at the final assimilation time, (a) observations, simulated with (b) CTRL, (c) RF, and (d) RFZDR.

Figure 10 shows the time evolution of the root-mean-square increment (RMSI) for the background and analysis for reflectivity and Zdr. The RMSI provides a quantitative measure of the overall magnitude of analysis adjustments introduced by data assimilation. For both reflectivity and Zdr, the RFZDR experiment generally exhibits larger RMSI values than the RF experiment throughout the assimilation window. This behavior indicates that the inclusion of Zdr leads to stronger analysis adjustments relative to reflectivity-only assimilation.

https://doi.org/10.5194/egusphere-2026-2230
Preprint. Discussion started: 27 July 2026

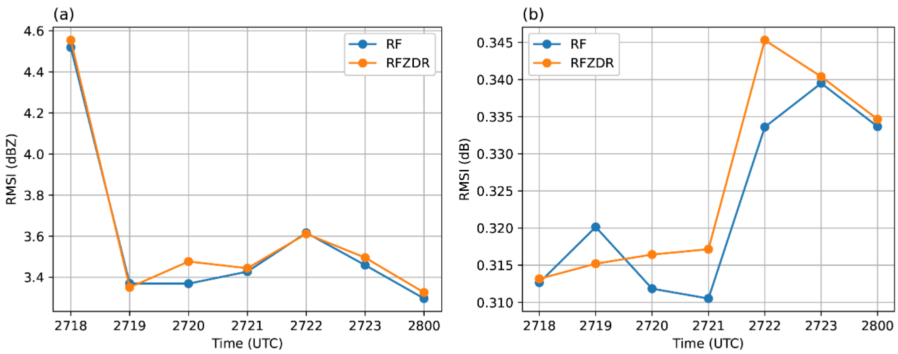

Figure 10 RMSI for (a) reflectivity and (b) Zdr.

To further examine the physical mechanisms underlying the initial assimilation effects, Fig. 11 presents vertical cross sections of hydrometeor analysis increments at the first assimilation time for the RF and RFZDR experiments. The increments of Qr are shown by shading, while Qg and Qs increments are indicated by green and red contours, respectively.

The vertical distributions of hydrometeor increments reveal a clear correspondence with the reflectivity adjustments shown in Fig. 6. In particular, the suppression of strong high-level reflectivity above the melting layer is primarily associated with negative snow mixing ratio increments, indicating a reduction of ice-phase hydrometeors in the upper-level region. This reduction is consistent with the decreased frequency of strong reflectivity at higher altitudes identified in the vertical cross sections.

In contrast, regions exhibiting stronger reflectivity in the RFZDR experiment relative to the RF experiment are mainly linked to positive rainwater mixing ratio increments below the melting layer. These enhanced rainwater increments indicate that the inclusion of Zdr leads to a more pronounced adjustment of rain-phase hydrometeors in the lower troposphere, which directly contributes to stronger reflectivity signatures at low levels.

https://doi.org/10.5194/egusphere-2026-2230
Preprint. Discussion started: 27 July 2026

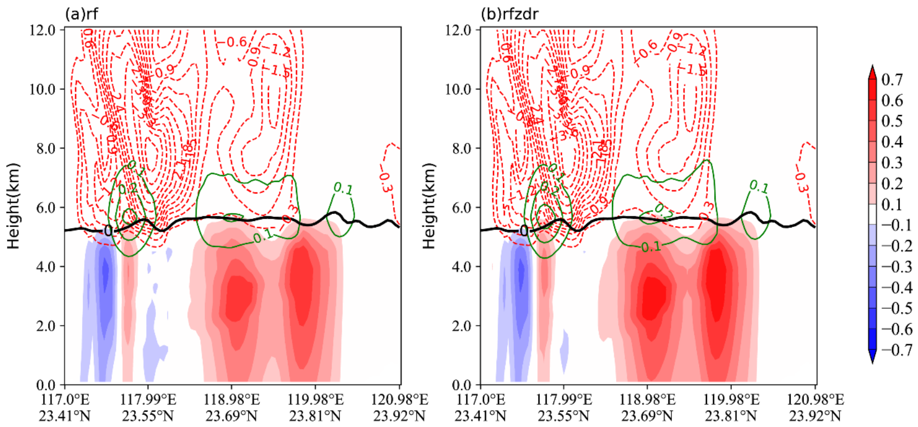

Figure 11 Hydrometeor analysis increments at 1800UTC for (a) RF and (b) RFZDR. Shading indicates qr (units: g/kg), green contours denote qg (units: g/kg), and red contours denote qs (units: g/kg).

Figure 12 presents the vertical cross section of hydrometeor mixing ratios along the black line in Fig. 8 at the final assimilation time. In the observations (Fig. 12a), the vertical hydrometeor structure exhibits a clear phase stratification. Below approximately 4 km, the hydrometeor is dominated by rainwater. Between 4 and 8 km, a mixed-phase region is evident, characterized by the coexistence of rain, graupel, and snow. Above 6 km, dry snow becomes the dominant hydrometeor type.

Compared to the CTRL experiment, both assimilation experiments substantially modify the hydrometeor distributions, yielding patterns that are generally consistent with the observations. Data assimilation increases the mixing ratios of rainwater and graupel and alters the vertical distribution of snow, particularly in the upper levels. The RFZDR experiment shows clear improvements over the RF experiment. In region A, it better reproduces the observed snow layer between 4 and 7 km and partially suppresses excessive graupel. These differences are physically consistent with the vertical structure of Zdr shown in Fig. 9. Because Zdr is primarily sensitive to rain-phase particles and wet snow in the melting layer, its assimilation provides additional constraints on the partitioning among rain, wet snow, and graupel. In region A, the higher Zdr values in Fig. 9(d) compared to Fig. 9(c) likely indicate an enhanced contribution from wet snow. This feature is consistent with the corresponding hydrometeor distributions in Fig. 12(d), where a more realistic mixture of rain and wet snow is evident. Accordingly, the enhanced rainwater mixing ratios in Fig. 12(c–d) correspond well to the high-Zdr regions in Fig. 9(c–d).

https://doi.org/10.5194/egusphere-2026-2230
Preprint. Discussion started: 27 July 2026

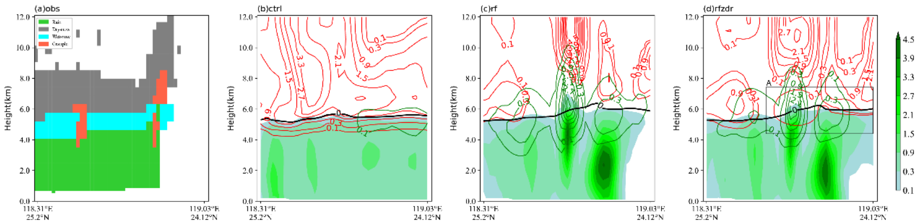

Figure 12 Hydrometeor distributions at the final assimilation time for (a) observations, (b) CTRL, (c) RF, and (d) RFZDR. Shading indicates qr (units: g/kg), green contours denote qg (units: g/kg), and red contours denote qs (units: g/kg).

The horizontal distributions of qr, qs, and qg at three representative model levels are examined in Fig. 13. Compared with the CTRL experiment, both the RF and RFZDR experiments exhibit substantial modifications to the hydrometeor distributions. Panels 13(a, d, g) show the hydrometeor distributions at the lower model level (level 5), where rainfall dominates near the surface, particularly within the spiral rainbands. At the intermediate model level (level 15), which is located near the melting layer, hydrometeors in all three phases—rain, snow, and graupel—coexist, reflecting mixed-phase microphysical processes. At this level, RFZDR produces enhanced rainwater within the spiral rainbands compared with RF, suggesting a stronger adjustment of rain-phase hydrometeors when Zdr information is assimilated. At the upper model level (level 20), snow becomes the dominant hydrometeor species. Both RF and RFZDR substantially reduce snow mixing ratios relative to the CTRL experiment, indicating an effective suppression of excessive ice-phase hydrometeors at higher altitudes through radar data assimilation.

https://doi.org/10.5194/egusphere-2026-2230
Preprint. Discussion started: 27 July 2026

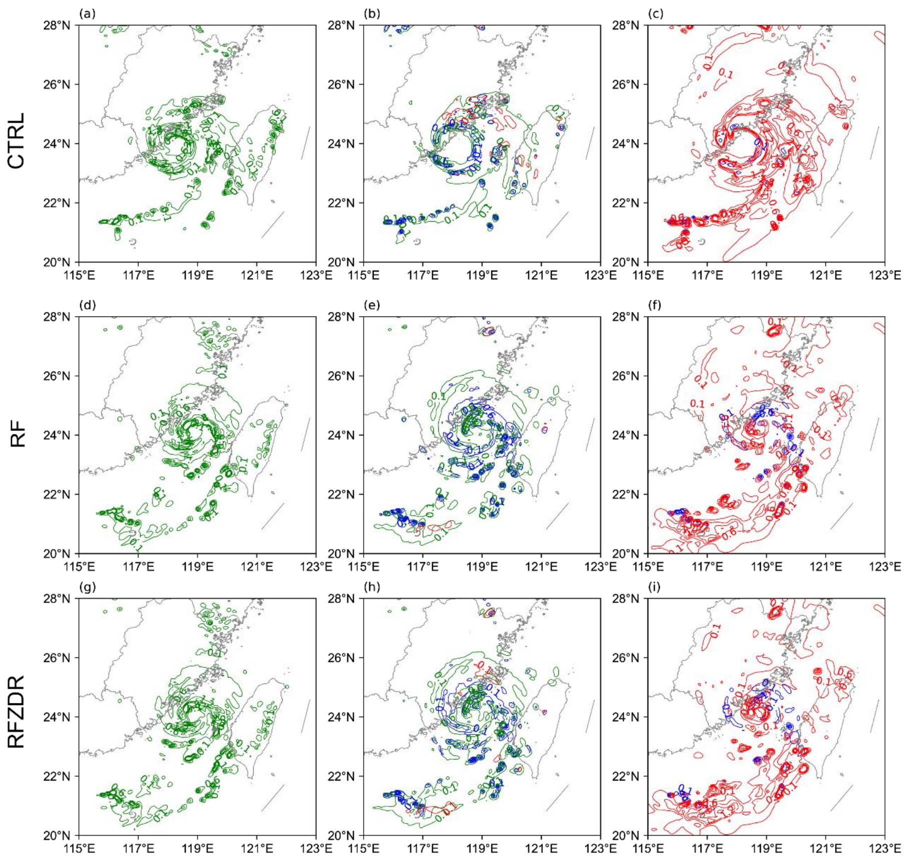

Figure 13 The distribution of hydrometeors at the final assimilation time. The first, second, and third columns correspond to model levels 5, 15, and 20, respectively. Green contours represent qr, blue contours represent qg, and red contours represent qs (units in g/kg).

4.2.2 Precipitation skill

Figure 14 displays the 3-h and 6-h accumulated precipitation forecasts, depicting the differences between the model forecasts and the observations. For both accumulation periods, the assimilation experiments exhibit noticeable displacements of the heavy precipitation regions and a general tendency to overestimate precipitation intensity in certain areas. Nevertheless, compared with the CTRL experiment, radar data assimilation leads to a marked improvement in both the location and overall intensity of the precipitation patterns.

For the 3-h accumulated precipitation, both the RF and RFZDR experiments tend to underestimate the observed rainfall amounts. Although the RF experiment exhibits a slightly smaller mean bias than RFZDR, the RFZDR experiment achieves a lower root-mean-square error (RMSE), indicating a more spatially consistent precipitation forecast. This suggests that the inclusion of Zdr information contributes to reducing localized forecast errors, even when the overall bias remains comparable.

https://doi.org/10.5194/egusphere-2026-2230
Preprint. Discussion started: 27 July 2026

In the 6-h accumulated precipitation, both RF and RFZDR underestimate the most intense precipitation exceeding 100 mm and slightly overestimate rainfall on the western side of the heavy precipitation region. Compared with RF, the RFZDR experiment partially suppresses this overestimation, resulting in reduced bias and RMSE. Consequently, RFZDR demonstrates improved overall forecast accuracy for accumulated precipitation, particularly in terms of spatial distribution and error consistency.

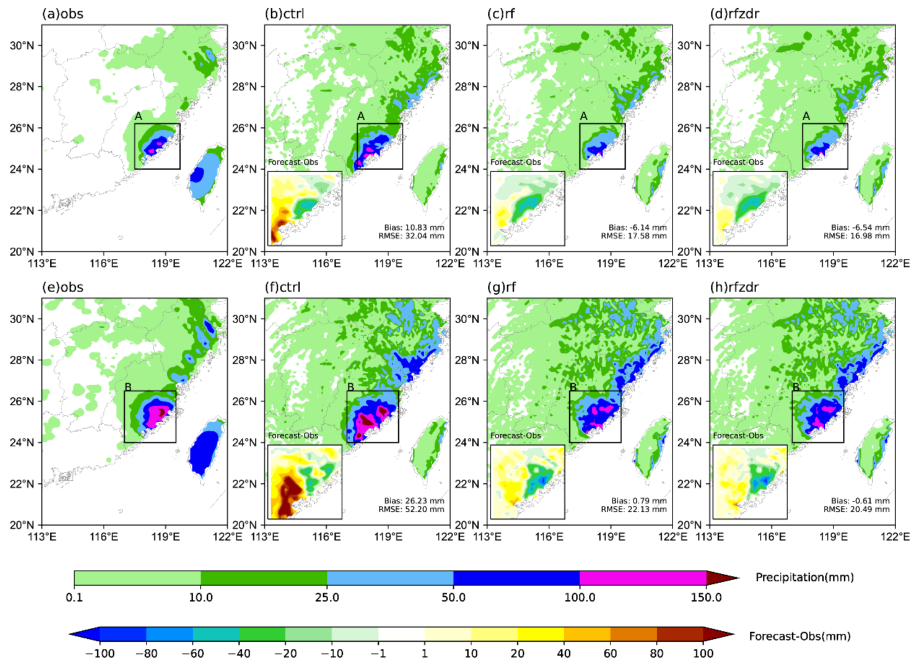

Figure 14 The first column shows 3-hour accumulated precipitation, while the second column shows 6-hour accumulated precipitation. The inset displays the difference between the model forecast and the observations. Panels (a, e) show observations, panels (b, f) show the CTRL experiment, panels (c, g) show the RF experiment, and panels (d, h) show the RFZDR experiment.

Figure 15 presents the Fractions Skill Score (FSS) and Equitable Threat Score (ETS) for 3-h (Fig. 15a) and 6-h (Fig. 15b) accumulated precipitation forecasts at thresholds of 10, 50, and 100 mm. For both accumulation periods, the RFZDR experiment generally achieves higher FSS and ETS scores than the RF and CTRL experiments across most thresholds, indicating an overall improvement in precipitation forecast skill when Zdr is assimilated. At lower thresholds (10 and 50 mm), the differences among the experiments are relatively modest, reflecting comparable performance in forecasting widespread. The improvement is particularly pronounced at the highest threshold of 100 mm, suggesting that RFZDR exhibits an enhanced capability in forecasting heavy rainfall events.

https://doi.org/10.5194/egusphere-2026-2230
Preprint. Discussion started: 27 July 2026

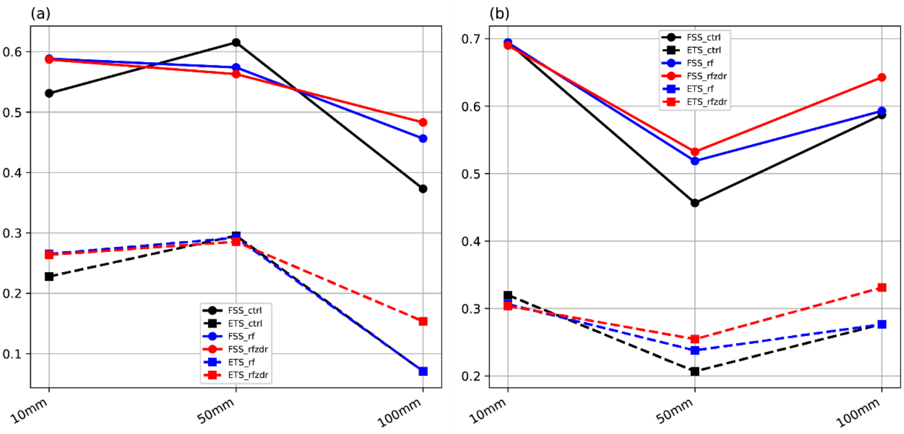

Figure 15 FSS and ETS scores are shown, with panel (a) representing 3-hour accumulated precipitation and panel (b) representing 6-hour accumulated precipitation.

5. Conclusions and Discussion

Building on the radar reflectivity observation operator developed by Wang and Liu (2018), this study develops a Zdr observation operator and integrates it into a variational data assimilation framework. In contrast to previous variational studies that primarily focused on warm-rain processes, the proposed operator systematically incorporates ice-phase hydrometeor and melting-layer contributions. Furthermore, the tangent linear and adjoint operators in the 3DVAR method were modified and extended to enable iterative calculations. The results demonstrate that the value of Zdr assimilation extends beyond simply introducing an additional observable. Instead, Zdr provides additional constraints on the suppression of spurious ice-phase echoes aloft, the phase partitioning near the melting layer, and the overall adjustment of precipitation structures.

The performance of the proposed Zdr assimilation approach is assessed in a typhoon case via both single-observation and cycling assimilation experiments. Results indicate that assimilating Zdr introduces additional microphysical constraints within the variational system. This yields a more effective adjustment of hydrometeor species relative to experiments that assimilate reflectivity alone. In the single-observation experiments, the RFZDR configuration produces stronger hydrometeor increments, indicating a more efficient suppression of excessive hydrometeor content when polarimetric information is included. These results demonstrate that Zdr provides complementary information to reflectivity, enabling a more complete constraint on the analyzed microphysical state.

In the cycling assimilation experiments, the RFZDR experiment yields a more physically consistent representation of reflectivity and Zdr compared with the RF experiment. The joint assimilation of reflectivity and Zdr results in a clearer suppression of excessive ice-phase hydrometeors aloft and a further enhancement of rain-phase hydrometeor at lower levels, thereby producing a more realistic vertical partitioning of hydrometeors.

https://doi.org/10.5194/egusphere-2026-2230
Preprint. Discussion started: 27 July 2026

These analysis improvements further propagate into short-term precipitation forecasts. Although biases in accumulated precipitation remain in both assimilation experiments, the RFZDR experiment consistently exhibits lower root-mean-square errors and improved spatial consistency relative to the RF experiment. Objective verification metrics, including FSS and ETS, indicate improved skill in heavy precipitation forecasts with the assimilation of ZDR. These improvements are more pronounced at higher thresholds, where the RFZDR experiment outperforms the RF experiment.

Overall, this study demonstrates that direct assimilation of Zdr within a variational framework improves the performance of data assimilation. This improvement is realized when the approach is combined with a polarimetric radar observation operator that accounts for ice-phase hydrometeors. The results highlight the importance of incorporating polarimetric information beyond reflectivity alone to better constrain microphysical processes and improve short-term forecasts of intense precipitation.

Several limitations of this study should be noted. First, the current implementation does not explicitly address uncertainties associated with microphysical parameterization schemes, nor does it account for the variability of intercept parameters during the assimilation cycle, both of which may contribute to residual biases. Second, the evaluation is limited to a single typhoon case. Future work will extend the proposed framework to a broader range of convective events and develop observation operators for additional polarimetric radar variables (e.g., Kdp). It will also evaluate the impact of different microphysical parameterization schemes on assimilation performance (Yao et al., 2025). Furthermore, efforts will be directed toward improving the consistency between the microphysics scheme and the observation operators to enhance overall assimilation efficiency (Zhang et al., 2021; Liu et al., 2024a).

Acknowledgments

This research was primarily supported by Open Research Foundation of Chongqing Key Laboratory of Numerical Model-AI Integrated Forecast and Warning for Severe Weather (MAIN-2025005), Beijige Funding from Nanjing Joint Institute for Atmospheric Sciences (BJG202503), the National Natural Science Foundation of China (41805070), Chongqing Natural Science Foundation Innovation and Development Joint Fund (CSTB2025NSCQ-QXLHJJZDX0008), the Open Grants of East China Phased Array Weather Radar Application Joint Laboratory (EPJF202503), the China Meteorological Administration Tornado Key Laboratory (TKL202306), Natural Science Fund of Anhui Province of China (2308085MD127). We acknowledge the High Performance Computing Center of Nanjing University of Information Science & Technology for their support of this work.

Code and data availability.

https://doi.org/10.5194/egusphere-2026-2230
Preprint. Discussion started: 27 July 2026

The modified code for RadDualIceVar v1.0 implemented in the WRFDA system, along with the experimental results presented in this study, are archived at https://zenodo.org/records/19689831 (Yi, 2026). The FNL data are available at https://gdex.ucar.edu/datasets/d083003/ (last access: April 2026) (National Centers for Environmental Prediction, National Weather Service et al., 2015). The raw Doppler radar and precipitation observations are provided by the Chinese Meteorological Administration and can be obtained via request at https://data.cma.cn/ (last access: April 2026).

Author contributions

LY performed validation, visualization, and writing (original draft preparation). FS contributed to methodology development and supervised this study. ZH contributed to software development and supervision. DX contributed to software development and writing (review and editing). All authors contributed to the writing of the manuscript.

Competing interests

The authors declare that they have no conflict of interest.

References

Bauer, P., Thorpe, A., and Brunet, G.: The quiet revolution of numerical weather prediction, *Nature*, **525**, 47–55, 2015.

Carlin, J. T., Gao, J., Snyder, J. C., and Ryzhkov, A. V.: Assimilation of ZDR columns for improving the spinup and forecast of convective storms in storm-scale models: Proof-of-concept experiments, *Mon. Weather Rev.*, **145**, 5033–5057, 2017.

Chen, H., Gao, J., Sun, T., Chen, Y., Wang, Y., and Carlin, J. T.: Assimilation of water vapor retrievals from ZDR columns using the 3DVar method for improving the short-term prediction of convective storms, *Mon. Weather Rev.*, **152**, 1077–1095, 2024.

Chen, J., Chen, Y., Zheng, H., et al.: Direct assimilation of dual-polarization radar using the hydrometeor background error covariance in the CMA-MESO model and its sensitivity to the microphysics scheme, *Adv. Atmos. Sci.*, **42**, 2153–2172, 2025.

Descombes, G., Auligné, T., Vandenberghe, F., Barker, D. M., and Barré, J.: Generalized background error covariance matrix model (GEN_BE v2.0), *Geosci. Model Dev.*, **8**, 669–696, 2015.

Dolan, B., Rutledge, S. A., Lim, S., Chandrasekar, V., and Thurai, M.: A robust C-band hydrometeor identification algorithm and application to a long-term polarimetric radar dataset, *J. Appl. Meteor. Climatol.*, **52**, 2162–2186, 2013.

Gao, J., and Stensrud, D. J.: Assimilation of reflectivity data in a convective-scale, cycled 3DVAR framework with hydrometeor classification, *J. Atmos. Sci.*, **69**, 1054–1065, 2012.

https://doi.org/10.5194/egusphere-2026-2230
Preprint. Discussion started: 27 July 2026

Ha, J.-H., and Lee, D.-K.: Effect of length scale tuning of background error in WRF-3DVAR system on assimilation of high-resolution surface data for heavy rainfall simulation, *Adv. Atmos. Sci.*, **29**, 1142–1158, 2012.

Hou, T., Kong, F., Chen, X., Lei, H., and Hu, Z.: Evaluation of radar and automatic weather station data assimilation for a heavy rainfall event in southern China, *Adv. Atmos. Sci.*, **32**, 967–978, 2015.

Iacono, M. J., Delamere, J. S., Mlawer, E. J., Shephard, M. W., Clough, S. A., and Collins, W. D.: Radiative forcing by long-lived greenhouse gases: Calculations with the AER radiative transfer models, *J. Geophys. Res.-Atmos.*, **113**, D13103, 2008.

Jimenez, P. A., Dudhia, J., Gonzalez-Rouco, J. F., Navarro, J., Montavez, J. P., and Garcia-Bustamante, E.: A revised scheme for the WRF surface layer formulation, *Mon. Weather Rev.*, **140**, 898–918, 2012.

Jung, Y., Zhang, G., and Xue, M.: Assimilation of simulated polarimetric radar data for a convective storm using the ensemble Kalman filter. Part I: Observation operators for reflectivity and polarimetric variables, *Mon. Weather Rev.*, **136**, 2228–2245, 2008.

Jung, Y., Xue, M., and Zhang, G.: Simulations of polarimetric radar signatures of a supercell storm using a two-moment bulk microphysics scheme, J. Appl. Meteor. Climatol., 49, 146–163, 2010.

Kain, J. S.: The Kain–Fritsch convective parameterization: An update, *J. Appl. Meteor.*, **43**, 170–181, 2004.

Kawabata, T., Schwitalla, T., Adachi, A., et al.: Observational operators for dual polarimetric radars in variational data assimilation systems (PolRad VAR v1.0), *Geosci. Model Dev.*, **11**, 2493–2501, 2018.

Liu, P., Gao, J., Zhang, G., and Carlin, J. T.: Assimilation of radar reflectivity data using parameterized forward operators for improving short-term forecasts of high-impact convection events, *J. Geophys. Res.-Atmos.*, **129**, e2024JD041458, 2024a.

Liu, P., Zhang, G., Carlin, J. T., and Gao, J.: A new melting model and its implementation in parameterized forward operators for polarimetric radar data simulation with double-moment microphysics schemes, *J. Geophys. Res.-Atmos.*, **129**, e2023JD040026, 2024b.

Louf, V., Protat, A., Jackson, R. C., Collis, S. M., and Helmus, J.: UNRAVEL: A robust modular velocity dealiasing technique for Doppler radar, *J. Atmos. Oceanic Technol.*, **37**, 741–758, 2020.

National Centers for Environmental Prediction, National Weather Service, NOAA, and U.S. Department of Commerce: NCEP GDAS/FNL 0.25 degree global tropospheric analyses and forecast grids, *NSF National Center for Atmospheric Research*, updated daily, 2015.

Parrish, D. F., and Derber, J. C.: The National Meteorological Center's spectral statistical-interpolation analysis system, *Mon. Weather Rev.*, **120**, 1747–1763, 1992.

Putnam, B. J., Jung, Y., Yussouf, N., et al.: The impact of assimilating ZDR observations on storm-scale ensemble forecasts of the 31 May 2013 Oklahoma storm event, *Mon. Weather Rev.*, **149**, 2021.

Shen, F., Xu, D., Li, H., and Liu, R.: Impact of radar data assimilation on a squall line over the Yangtze–Huaihe River basin with a radar reflectivity operator accounting for ice-phase hydrometeors, *Meteorol. Appl.*, **28**, e1967, 2021.

Shen, F., and Min, J.: Assimilating AMSU-A radiance data with the WRF hybrid En3DVAR system for track predictions of Typhoon Megi (2010), *Adv. Atmos. Sci.*, **32**, 1231–1243, 2015.

Snyder, J. C., Bluestein, H. B., Zhang, G., and Frasier, S. J.: Attenuation correction and hydrometeor classification of high-resolution, X-band, dual-polarized mobile radar measurements in severe convective storms, *J. Atmos. Oceanic Technol.*, **27**, 1979–2001, 2010.

Snyder, J. C., and Ryzhkov, A. V.: Automated detection of polarimetric tornadic debris signatures using a hydrometeor classification algorithm, *J. Appl. Meteor. Climatol.*, **54**, 1861–1870, 2015.

Tabary, P., Boumahmoud, A.-A., Andrieu, H., Thompson, R. J., Illingworth, A. J., Le Bouar, E., and Testud, J.: Evaluation of two integrated polarimetric quantitative precipitation estimation (QPE) algorithms at C-band, *J. Hydrol.*, **405**, 248–260, 2011.

Tewari, M., Chen, F., Wang, W., Dudhia, J., LeMone, M. A., Mitchell, K., Ek, M., Gayno, G., Wegiel, J., and Cuenca, R. H.: Implementation and verification of the unified NOAH land surface model in the WRF model, *Proc. 20th Conf. Weather Analysis and Forecasting/16th Conf. Numerical Weather Prediction*, 11–15, 2004.

Thompson, G., Rasmussen, R. M., and Manning, K.: Explicit forecasts of winter precipitation using an improved bulk microphysics scheme. Part I: Description and sensitivity analysis, *Mon. Weather Rev.*, **132**, 519–542, 2004.

Wang, H., Sun, J., Fan, S., and Huang, X.-Y.: Indirect assimilation of radar reflectivity with WRF 3D-Var and its impact on prediction of four summertime convective events, *J. Appl. Meteor. Climatol.*, **52**, 889–902, 2013.

Wang, M., Zhao, K., Xue, M., et al.: Precipitation microphysics characteristics of a Typhoon Matmo (2014) rainband after landfall over eastern China based on polarimetric radar observations, *J. Geophys. Res.-Atmos.*, **121**, 2016JD025307, 2016.

Wang, S., and Liu, Z.: A radar reflectivity operator with ice-phase hydrometeors for variational data assimilation (version 1.0) and its evaluation with real radar data, *Geosci. Model Dev.*, **12**, 4031–4051, 2019.

Wu, D., Zhao, K., Kumjian, M. R., et al.: Kinematics and microphysics of convection in the outer rainband of Typhoon Nida (2016) revealed by polarimetric radar, *Mon. Weather Rev.*, **146**, 2147–2159, 2018.

Xiao, Q., and Sun, J.: Multiple-radar data assimilation and short-range quantitative precipitation forecasting of a squall line observed during IHOP_2002, *Mon. Weather Rev.*, **135**, 3381–3404, 2007.

Yao, F., Li, X., Qin, Z., Chen, G., and Dong, X.: Effect of microphysical schemes on simulating severe convection induced by the northeast cold vortex using dual-polarization radar data, *Meteorol. Atmos. Phys.*, **137**, 17, 2025.

Yi, L.: Development of a dual-polarization Zdr radar operator with ice-phase hydrometeor classification for variational assimilation systems, Zenodo [data set],https://zenodo.org/records/19689831, 2026.

https://doi.org/10.5194/egusphere-2026-2230
Preprint. Discussion started: 27 July 2026

Zhang, G., Vivekanandan, J., and Brandes, E.: A method for estimating rain rate and drop size distribution from polarimetric radar measurements, *IEEE Trans. Geosci. Remote Sens.*, **39**, 830–841, 2001.

Zhang, G., Mahale, V. N., Putnam, B. J., et al.: Current status and future challenges of weather radar polarimetry: Bridging the gap between radar meteorology, hydrology, engineering and numerical weather prediction, *Adv. Atmos. Sci.*, **36**, 571–588, 2019.

Zhang, G., Gao, J., and Du, M.: Parameterized forward operators for simulation and assimilation of polarimetric radar data with numerical weather predictions, *Adv. Atmos. Sci.*, **38**, 737–754, 2021.